

X-RAY AND OPTICAL CORRELATION OF TYPE I SEYFERT NGC 3516 STUDIED WITH *SUZAKU* AND JAPANESE GROUND-BASED TELESCOPES

HIROFUMI NODA^{1,2}, TAKEO MINEZAKI³, MAKOTO WATANABE^{4,14}, MITSURU KOKUBO^{3,5}, KENJI KAWAGUCHI⁶, RYOSUKE ITOH⁶, KUMIKO MORIHANA⁷, YOSHIHIKO SAITO⁸, HIKARU NAKAO⁴, MASATAKA IMAI⁴, YUKI MORITANI⁹, KATSUTOSHI TAKAKI⁶, MIHO KAWABATA⁶, TATSUYA NAKAOKA⁶, MAKOTO UEMURA¹⁰, KOJI KAWABATA¹⁰, MICHITOSHI YOSHIDA¹⁰, AKIRA ARAI^{7,15}, YUHEI TAKAGI⁷, TOMOKI MOROKUMA³, MAMORU DOI³, YOICHI ITOH⁷, SHIN'YA YAMADA¹¹, KAZUHIRO NAKAZAWA¹², YASUSHI FUKAZAWA⁶, AND KAZUO MAKISHIMA^{12,13}

Submitted 2016 February 6, Accepted 2016 May 23

ABSTRACT

From 2013 April to 2014 April, we performed an X-ray and optical simultaneous monitoring of the type 1.5 Seyfert galaxy NGC 3516. It employed *Suzaku*, and 5 Japanese ground-based telescopes, the Pirka, Kiso Schmidt, Nayuta, MITSuME, and the Kanata telescopes. The *Suzaku* observations were conducted seven times with various intervals ranging from days, weeks, to months, with an exposure of ~ 50 ksec each. The optical *B*-band observations not only covered those of *Suzaku* almost simultaneously, but also followed the source as frequently as possible. As a result, NGC 3516 was found in its faint phase with the 2–10 keV flux of $0.21\text{--}2.70 \times 10^{-11}$ erg s⁻¹ cm⁻². The 2–45 keV X-ray spectra were composed of a dominant variable hard power-law continuum with a photon index of ~ 1.7 , and a non-relativistic reflection component with a prominent Fe-K α emission line. Producing the *B*-band light curve by differential image photometry, we found that the *B*-band flux changed by $\sim 2.7 \times 10^{-11}$ erg s⁻¹ cm⁻², which is comparable to the X-ray variation, and detected a significant flux correlation between the hard power-law component in X-rays and the *B*-band radiation, for the first time in NGC 3516. By examining their correlation, we found that the X-ray flux preceded that of *B* band by $2.0^{+0.7}_{-0.6}$ days (1σ error). Although this result supports the X-ray reprocessing model, the derived lag is too large to be explained by the standard view which assumes a “lamppost”-type X-ray illuminator located near a standard accretion disk. Our results are better explained by assuming a hot accretion flow and a truncated disk.

Subject headings: galaxies: active – galaxies: individual (NGC 3516) – galaxies: Seyfert – X-rays: galaxies

1. INTRODUCTION

¹ Frontier Research Institute for Interdisciplinary Sciences, Tohoku University, 6-3 Aramaki-zaaoba, Aoba-ku, Sendai, Miyagi 980-8578, Japan, e-mail: hirofumi.noda@astr.tohoku.ac.jp

² Astronomical Institute, Tohoku University, 6-3 Aramaki-zaaoba, Aoba-ku, Sendai, Miyagi 980-8578, Japan

³ Institute of Astronomy, School of Science, The University of Tokyo, Mitaka, Tokyo 181-0015, Japan

⁴ Department of CosmoSciences, Hokkaido University, Kita 10, Nishi 8, Kita-ku, Sapporo, Hokkaido 060-0810, Japan

⁵ Department of Astronomy, School of Science, the University of Tokyo, 7-3-1 Hongo, Bunkyo-ku, Tokyo 113-0033, Japan

⁶ Department of Physical Science, Hiroshima University, 1-3-1 Kagamiyama, Higashi-Hiroshima, Hiroshima 739-8526, Japan

⁷ Nishi-harima Astronomical Observatory, Center for Astronomy, University of Hyogo, 407-2 Nichigaichi, Sayo-cho, Sayo, Hyogo 670-5313, Japan

⁸ Department of Physics, Tokyo Institute of Technology, 2-12-1 Ookayama, Meguro-ku, Tokyo 152-8551, Japan

⁹ Kavli Institute for the Physics and Mathematics of the Universe (Kavli IPMU), The University of Tokyo, 5-1-5 Kashiwanoha, Kashiwa 277-8583, Japan

¹⁰ Hiroshima Astrophysical Science Center, Hiroshima University, Higashi-Hiroshima, Hiroshima 739-8526, Japan

¹¹ Department of Physics, Tokyo Metropolitan University, 1-1 Minami-Osawa, Hachioji, Tokyo 192-0397 Japan

¹² Department of Physics, School of Science, The University of Tokyo, 7-3-1 Hongo, Bunkyo-ku, Tokyo 113-0033, Japan

¹³ MAXI Team, Global Research Cluster, RIKEN, Wako, Saitama 351-0198, Japan

¹⁴ Department of Applied Physics, Okayama University of Science, 1-1, Ridai-cho, Kita-ku, Okayama 700-0005, Japan

¹⁵ Koyama Astronomical Observatory, Kyoto Sangyo University, Motoyama, Kamigamo, Kita-ku, Kyoto 603-8555, Japan

An Active Galactic Nucleus (AGN) is known to generate multi-wavelength radiation by mass accretion onto a Super Massive Black Hole (SMBH) in its central engine. An important element of the central engine is the standard accretion disk (e.g., Shakura & Sunyaev 1973; Balbus & Hawley 1991; Machida 2000), which is expected to form at the Eddington ratio of $L_{\text{bol}}/L_{\text{Edd}} \sim 0.1\text{--}1$ (e.g., Abramowicz et al. 1995), and converts appreciable fraction of the gravitational energy release of the accreting matter into optically-thick radiation. A part of the radiation has been observed as “big blue bump” seen in optical spectra from AGNs that have disk radiation stronger than jet emission, like Seyfert galaxies and quasars (e.g., Elvis et al. 1994).

The central engine requires another element that boosts up these low-energy photons into the observed X-ray signals. This is usually attributed to some sort of hot Maxwellian electrons, or “corona”, which Compton-upscatter the seed photons into broadband X-ray photons. However, the configuration of such corona is still under big debates, in contrast to the well-understood standard accretion disk. Some X-ray studies led to an argument that a compact corona is located on a rotation axis of the accretion disk like a “lamppost”, producing an extremely relativistically-broadened reflection component by illuminating the inner accretion disk (e.g., Miniutti & Fabian 2004; Dauser et al. 2013). Others argue that an extended corona is present at the inner edge of an accretion disk, sometimes affected by partially-covering

absorptions of ionized matters (e.g., Miller et al. 2008; Miyakawa et al. 2012). To settle the scenario of the Comptonizing corona, we need to focus on primary X-ray spectra and their flux variability.

According to X-ray studies of AGNs, several kinds of primary X-ray signals with distinct spectral and timing properties were reported. A flat primary spectrum, which is reproduced by a single Power-Law (PL) continuum with the photon index of $\Gamma \lesssim 1.7$, dominates in X-rays from relatively low Eddington-ratio AGNs (e.g., Terashima et al. 2002). On the other hand, a steep primary continuum, which can be explained by a PL model with $\Gamma \gtrsim 2.3$, is dominant in X-rays from highly-accreting AGNs like narrow-line type 1 Seyferts (e.g., Laor et al. 1994; Boller et al. 1996). Recently, Noda et al. (2011a, 2013a, and 2014) revealed that both these flat and steep primary continua are simultaneously present in the X-ray emission from multiple Seyfert galaxies. The presence of these different primary X-rays may represent presence of several distinct types of coronae with different electron temperatures and optical depths. Furthermore, in order to explain a soft X-ray excess structure at a low energy band below ~ 3 keV, a soft thermal Comptonization continuum has been suggested, invoking yet another corona (e.g., Mehdipour et al. 2011; Noda et al. 2011b, 2013b; Jin et al. 2013). The reality of this third corona, however, needs further examination, because the soft excess may alternatively be modeled in terms of relativistically-smearing ionized reflection (e.g., Fabian et al. 2004) or absorption by disk winds (e.g., Cierlinski & Done 2004).

To clarify geometry of materials around a SMBH, correlations and time lags between emissions in different energy bands are useful. Recently, studies of reverberation between different X-ray bands revealed that soft X-rays and Fe-K α emission lines have positive time lags, by hundreds seconds, against hard X-rays, with an implication that some reprocessing materials are present near the hard X-ray emitters (e.g., Uttley et al. 2014). Likewise, X-ray and optical/ultraviolet (UV) correlations are useful to investigate coronal geometries around an accretion disk. Because seed photons for the inverse Comptonization process are presumably provided via the optical/UV disk black body, variations in these low-energy bands can precede that of X-rays with a lag of \sim days (e.g., Nandra et al. 2000). When fluctuations of the mass accretion rate propagate inward from the accretion disk to the corona, the optical emission is also expected to precede X-rays, but on a viscous or thermalizing time scale which may be much longer than days (e.g., Uttley & Casella 2014). On the other hand, the disk should be illuminated by the X-rays, so that X-ray variations can cause optical flux changes, producing delays of \sim days in the opposite sense (e.g., Krolik et al. 1991). In order to distinguish these cases, and to better understand the geometry of the coronae and accretion disk, we need to measure the sign and length of the optical vs. X-ray time lag, and quantify the strength of their correlations.

So far, a large amount of effort has been invested on coordinated X-ray and optical/UV observations of a number of AGNs. However, we are far from achieving a unified view. For example, Seyfert galaxies including NGC 5548 (Uttley et al. 2003; Suganuma et al. 2006; McHardy et al. 2014), NGC 3783 (Arevalo et

al. 2009), and Mrk 79 (Breedt et al. 2000) exhibited relatively strong correlations with optical lags by several days, while those including Ark 564 (Gaskell 2006) and NGC 3516 (Maoz et al. 2002) showed much poorer correlations. One possible cause of this variety, we speculate, is that the different X-ray primary continua have different correlations to the optical/UV signals, and the previous coordinated observations mixed up the effects from these multiple X-ray components. To overcome this difficulty, simultaneous observations of AGNs should be conducted, under a condition wherein the different X-ray components can be clearly identified and separated.

To derive the geometrical information from the multi-wavelength correlations, we performed an X-ray and optical simultaneous monitoring during 2013–2014, by utilizing *Suzaku* (Mitsuda et al. 2007) and 5 Japanese ground-based telescopes. The target of this campaign is the bright type 1.5 Seyfert galaxy NGC 3516. It has a redshift of $z = 0.00884$ which corresponds to a distance of $D = 41.3$ Mpc $= 1.3 \times 10^{26}$ cm. Its SMBH is estimated to have a mass of $M_{\text{BH}} = 3.2 \times 10^7 M_{\odot}$ (Denney et al. 2010), which yields the Schwarzschild radius of $R_{\text{S}} = 0.95 \times 10^{13}$ cm. The column density of the Galactic interstellar absorption toward NGC 3516 is $N_{\text{H}} = 4.08 \times 10^{20}$ cm $^{-2}$ (Dickey & Lockman 1990), and the optical Galactic extinction is $A_B = 0.151$ mag (NASA/IPAC Extragalactic Database based on Schlafly & Finkbeiner 2011). Although NGC 3516 was previously reported, by Maoz et al. (2002), to exhibit a poor X-ray and optical correlation, the result will change if we properly decompose its X-ray continuum using the technique of Noda et al. (2011b, 2013b), because NGC 3516 is one of the prototypical objects to which this method has been successfully applied (Noda et al. 2013). Unless otherwise stated, errors shown in tables and figures in the present paper refer 1σ errors.

2. OBSERVATION AND DATA REDUCTION

2.1. X-ray

The X-ray monitoring observations of NGC 3516 were performed in the *Suzaku* AO-8 cycle during 2013–2014. Specifically, NGC 3516 was observed with *Suzaku* five times from 2013 April 10 to May 29, with intervals of ~ 1 –2 weeks. Another pointing was carried out on November 7, and the last one on 2014 April 4; thus, total 7 observations, with various intervals from days to months. In the present paper, we call the 1st, 2nd, ... and the 7th observations epoch 1, epoch 2, ... and epoch 7, respectively. The exposure in each epoch was ~ 50 ksec, except for epoch 2 which has an exposure of ~ 20 ksec. In all these epochs, the XIS (Koyama et al. 2007) and HXD (Takahashi et al. 2007) were operated in their normal modes, and data of the XIS and HXD-PIN are utilized in the present paper, except for epoch 7, in which the HXD-PIN count rate was too low to significantly detect the signals.

The data of the XIS and HXD-PIN were processed via the software version 2.4. In the XIS analysis, we added the data of XIS0 and XIS3, and utilized it as FI data, while we did not use XIS1 due to its higher background. The XIS source events were extracted from a $120''$ -radius circle with its center on the source. Background events were accumulated from a surrounding an-

TABLE 1
X-RAY OBSERVATIONS BY *Suzaku*

Epoch	Observation Start (UT)	End (UT)	Middle (MJD)	Exposure Time (ksec)
1	2013 Apr 9 23:13:20	Apr 11 01:06:16	56392.51	51
2	2013 Apr 27 00:17:13	Apr 27 10:42:22	56409.27	19
3	2013 May 12 00:22:24	May 13 02:30:23	56424.58	50
4	2013 May 23 03:32:08	May 24 07:05:07	56435.72	51
5	2013 May 29 11:02:50	May 30 15:15:14	56442.05	54
6	2013 Nov 4 06:15:13	Nov 5 05:10:17	56600.74	46
7 ^a	2014 Apr 7 16:54:26	Apr 8 12:00:24	56755.12	52

^a Only the XIS data are utilized.

TABLE 2
TELESCOPES AND INSTRUMENTS FOR THE OPTICAL OBSERVATIONS

Telescope	Mirror Diameter (m)	Instrument	Field of View (arcmin)	Pixel Scale (arcsec pixel ⁻¹)	Observing Band	n_{obs} ^a
Pirka	1.6	MSI ^b	3.3×3.3	0.39	B, V	86
MITSuME	0.5	MITSuME ^c	28×28	1.64	g', R_C, I_C	6
Kiso Schmidt	1.5	KWFC ^d	60×30 ^e	0.95	B, V	32
Nayuta	2.0	MINT ^f	11×11	0.32	B, V	31
Kanata	1.5	HOWPol ^g	ϕ_{15}	0.29	B, V	31

^a The total number of observing nights.

^b Multi-Spectral Imager (MSI; Watanabe et al. 2012).

^c Multicolor Imaging Telescopes for Survey and Monstrous Explosions (MITSuME; Kotani et al. 2005).

^d Kiso Wide Field Camera (KWFC; Sako et al. 2012).

^e Only one of the eight CCDs installed in KWFC was used.

^f Multiband Imager for Nayuta Telescope (MINT; Ozaki et al. 2005).

^g Hiroshima One-shot Wide-field Polarimeter (HOWPol; Kawabata et al. 2008).

nular region with the inner radius of $180''$ and the outer radius of $270''$. The response and ancillary-response files were prepared via softwares in HEASOFT 6.14 called *xisrmfgen* and *xissimarfgen* (Ishisaki et al. 2007), respectively. The HXD data were prepared by the same way as that of the XIS. In the HXD analysis, Non X-ray Background (NXB) and Cosmic X-ray Background (CXB) were estimated by standard models described by Fukazawa et al. (2009) and Gruber et al. (1999), respectively. They were subtracted from the on-source data.

2.2. Optical

The optical photometric monitoring observations of NGC 3516 were performed by using the charge-coupled device (CCD) cameras installed at the Pirka, MITSuME, Kiso Schmidt, Nayuta, and Kanata telescopes, of which major parameters are summarized in Table 2. Simultaneous monitoring observations were performed at the same 7 epochs as the X-ray observations by *Suzaku*. In addition, from 2013 January to 2014 April, these telescopes densely monitored the source even without the simultaneous X-ray coverage, with a typical intervals of ~ 1 day. In the present paper, we present the B - and the g' -bands photometric data, because the optical continuum emission of AGNs is generally bluer than that of the host galaxy, thus ensuring better sensitivity to the

AGN signals. The images were reduced using IRAF¹⁶ following the standard procedures of image reduction for CCD detectors.

3. DATA ANALYSIS AND RESULTS

3.1. X-ray Light Curves and Spectra

Figure 1 shows light curves in the 2–3 keV and 3–10 keV bands in all the 7 epochs. While we can see gradual flux changes, the source did not show short-term variations, on time scales of \sim hours, that were observed by *XMM-Newton* in 2006 (Mehdipour et al. 2010). The 2–3 keV light curves are clearly synchronized with that in the 3–10 keV band. The highest flux was obtained in epoch 4, while the lowest in epoch 7, with a peak to peak variation amplitude reaching a factor of ~ 20 . To quantify the flux variability, we made, in Figure 2, a count-count plot between count rates in the 2–3 keV and 3–3.5 keV bands, where these objects generally exhibit rather high variability (Noda et al. 2013a). The count-count plot of NGC 3516 derived in 2009 October (Noda et al. 2013c) is also shown for reference, after correcting the data for a pointing position difference and long-term changes in the detector response. Surprisingly, all the data points in 2013–2014 line up with those in

¹⁶ IRAF is distributed by the National Optical Astronomy Observatories, which are operated by the Association of Universities for Research in Astronomy, Inc., under cooperative agreement with the National Science Foundation.

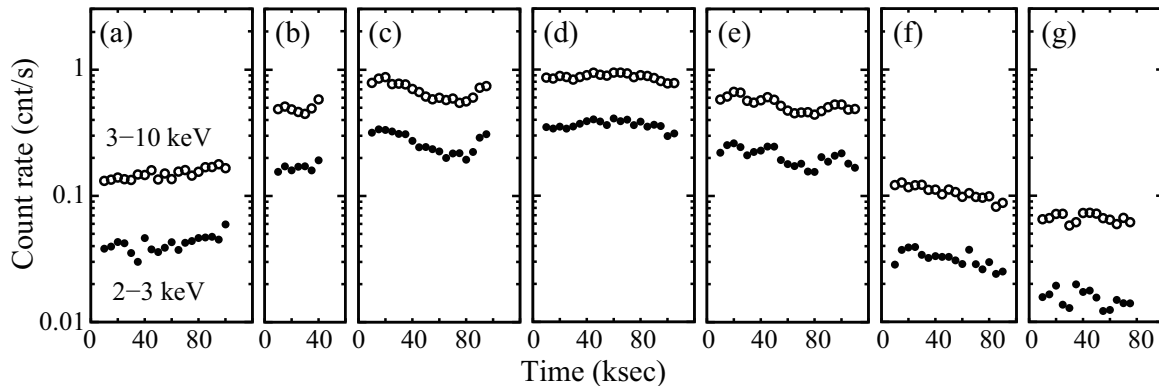


FIG. 1.— XIS light curves of NGC 3516 in the 2–3 keV (open circles) and 3–10 keV (filled circles) bands, binned into 5 ksec, in epoch 1 (panel a), 2 (panel b), 3 (panel c), 4 (panel d), 5 (panel e), 6 (panel f), and 7 (panel g). The error bars are all within 0.01 cnt s^{-1} in both bands, and are hence omitted.

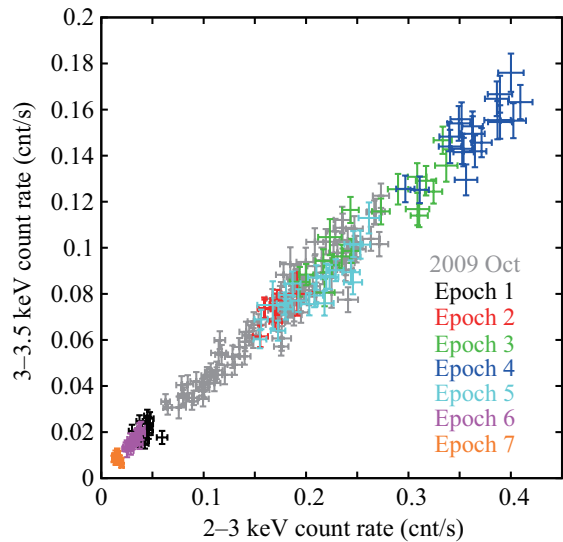


FIG. 2.— A count-count plot between the 2–3 keV and 3–3.5 keV count rates, binned into 5 ksec. Black, red, green, blue, cyan, purple and orange indicate epoch 1, 2, 3, 4, 5, 6, and 7, respectively. Grey shows the data on 2009 October 28, which is same as those in Noda et al. (2013c), but corrected for the difference of the pointing position and some response changes from 2009 to 2013.

2009, thus defining an almost linear correlation between the two bands. This means that the variable component in those energy bands observed in 2013–2014 has nearly the same spectral shape to that detected in 2009.

In energy bands higher than 3.5 keV, a reflection component with a prominent Fe-K α emission line at ~ 6.4 keV is expected to become more dominant than in energies below 3.5 keV. Therefore, this variable component should be separated from the reflection via spectral fitting. Although the reflection component is considered almost stationary within a week (Noda et al. 2013b), it can vary on timescales of months, because a broad line region and/or a dusty torus, where the reflection emission possibly originates, are known to locate at sev-

eral tens–hundreds light days (e.g., Koshida et al. 2014). Accordingly, we treat the reflection signal as a variable component.

As presented in Figure 3, we produced seven time-averaged and background-subtracted spectra, one from each epoch, and performed a simultaneous model fitting to them. Because of the presence of diffuse X-ray emissions in the host galaxy (e.g., Constantini et al. 2000; George et al. 2002), and effects of absorption variations (e.g., Turner et al. 2011), we ignored energy bands lower than 2 keV, and utilized the 2–45 keV energies in each spectrum. The employed spectral model is `wabs * (cutoffpl + pexmon)` in XSPEC12, which is consistent with that utilized in Noda et al. (2013a, c). Here, `wabs` is a model for the photoelectric absorption (Morrison and McCammon 1983), and its column density N_{H} was allowed to differ among the epochs. The `cutoffpl` model represents the PL continuum with a high energy exponential rolloff, utilized to emulate the inverse Comptonization radiation. The reflection continuum and the Fe-K α emission line, both produced by this continuum, are reproduced by `pexmon` (Nandra et al. 2007).

In the fitting, the photon index Γ was tied among the epochs (because of Figure 2), and left free. The cutoff energy E_{cut} was fixed at 150 keV based on the typical value reported by Malizia et al. (2014), while the normalization N_{PL} was left free in each epoch. For `pexmon`, Γ and E_{cut} of the incident PL were tied to those in `cutoffpl`, and the Fe abundance A_{Fe} , inclination angle I , and the reflection fraction f_{ref} were fixed at 1 Solar, 60° , and 1, respectively. The normalization N_{ref} of the `pexmon` component was allowed to differ among the epochs. The N_{ref} value is determined almost solely by the Fe-K α line intensity, because the ratio between the Fe-K α line intensity and the reflection continuum in `pexmon` does not change when E_{cut} , A_{Fe} , and I are all fixed. As summarized in Figure 3 and Table 3, the simultaneous fitting was successful with $\chi^2/\text{d.o.f.}=1184.0/1113$. As expected from Figure 2, all the spectra have been reproduced by a hard PL continuum having $\Gamma \sim 1.75$, which is consistent with that in 2009 ($\Gamma = 1.72^{+0.08}_{-0.12}$), together with a reflection

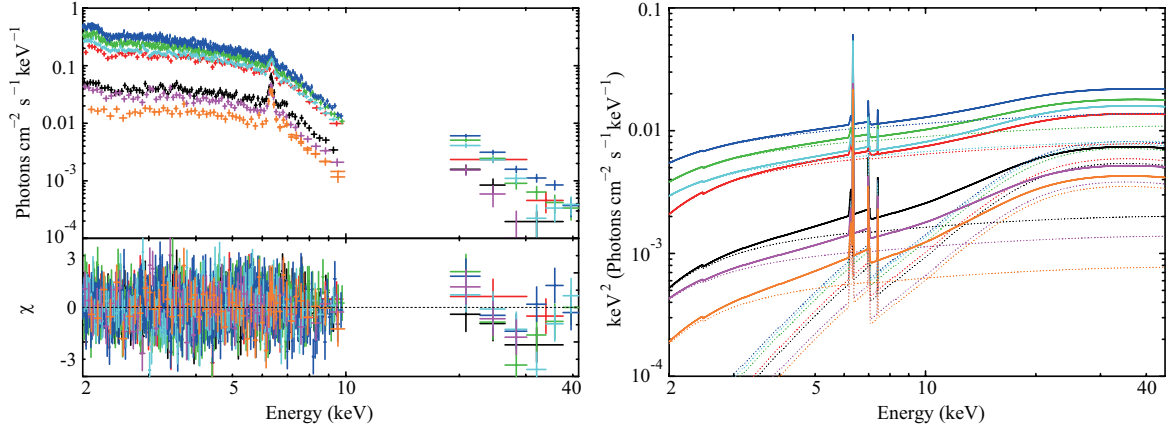


FIG. 3.— The 2–45 keV time-averaged spectra, of which the epochs are specified by the same color as in Figure 2. They are fitted simultaneously with the model of `wabs * (cutoffpl + pexmon)` in XSPEC12. Left panel shows the spectra including the XIS and XRD-PIN detector responses (top) and residuals from the model (bottom). Right panel shows unfolded best-fit model spectra in a νF_ν form.

TABLE 3
PARAMETERS OBTAINED BY THE SIMULTANEOUS FITTING TO ALL THE 2–45 KEV TIME-AVERAGED SPECTRA

Component	Parameter	Epoch 1	Epoch 2	Epoch 3	Epoch 4	Epoch 5	Epoch 6	Epoch 7
wabs	N_{H}^{a}	$1.93^{+0.14}_{-0.15}$	$1.86^{+0.10}_{-0.11}$	$1.21^{+0.06}_{-0.07}$	$0.94^{+0.05}_{-0.06}$	1.16 ± 0.07	$1.52^{+0.16}_{-0.17}$	$2.10^{+0.21}_{-0.25}$
cutoffpl	Γ_{PL}				$1.75^{+0.01}_{-0.02}$			
	$E_{\text{cut, PL}}$ (keV)				150 (fix)			
	N_{PL}^{b}	$1.00^{+0.02}_{-0.03}$	$3.94^{+0.11}_{-0.13}$	$5.44^{+0.09}_{-0.12}$	$6.93^{+0.12}_{-0.15}$	$4.10^{+0.07}_{-0.09}$	$0.69^{+0.02}_{-0.03}$	0.39 ± 0.02
	F_{PL}^{c}	0.37 ± 0.01	$1.44^{+0.04}_{-0.05}$	$1.99^{+0.03}_{-0.04}$	$2.53^{+0.04}_{-0.05}$	$1.50^{+0.02}_{-0.03}$	0.25 ± 0.01	0.14 ± 0.01
pexmon	Γ_{ref}				$=\Gamma_{\text{PL}}$			
	$E_{\text{cut, ref}}$ (keV)				$=E_{\text{cut, PL}}$			
	f_{ref}				1 (fix)			
	$A_{\text{Fe}} (Z_{\odot})$				1 (fix)			
	$N_{\text{ref}}^{\text{d}}$	$3.88^{+0.25}_{-0.26}$	$4.24^{+0.51}_{-0.50}$	$5.17^{+0.42}_{-0.44}$	$5.88^{+0.47}_{-0.49}$	$5.60^{+0.40}_{-0.41}$	2.73 ± 0.21	2.51 ± 0.18
	$F_{\text{ref}}^{\text{e}}$	1.10 ± 0.07	$1.20^{+0.15}_{-0.14}$	1.46 ± 0.12	$1.67^{+0.13}_{-0.14}$	$1.59^{+0.11}_{-0.12}$	0.78 ± 0.06	0.71 ± 0.05
	$F_{\text{total}}^{\text{f}}$	0.48 ± 0.04	1.56 ± 0.07	$2.14^{+0.06}_{-0.07}$	2.70 ± 0.07	$1.66^{+0.05}_{-0.06}$	0.33 ± 0.03	0.21 ± 0.02
$\chi^2/\text{d.o.f.}$					1184.0/1113			

NOTE. — The errors refer to 1σ confidence ranges.

^a Equivalent hydrogen column density in 10^{22} cm^{-2} .

^b The power-law normalization at 1 keV, in units of $10^{-3} \text{ photons keV}^{-1} \text{ cm}^{-2} \text{ s}^{-1}$ at 1 keV.

^c The 2–10 keV flux of the PL component without being absorbed, in units of $10^{-11} \text{ erg cm}^{-2} \text{ s}^{-1}$.

^d The `pexmon` normalization at 1 keV, in units of $10^{-3} \text{ photons keV}^{-1} \text{ cm}^{-2} \text{ s}^{-1}$ at 1 keV.

^e The 2–10 keV flux of the reflection component without being absorbed, in units of $10^{-12} \text{ erg cm}^{-2} \text{ s}^{-1}$.

^f The 2–10 keV total flux without being absorbed in units of $10^{-11} \text{ erg cm}^{-2} \text{ s}^{-1}$, calculated as a sum of F_{PL} and F_{ref} .

component accompanied by a prominent Fe-K α emission line. Although N_{H} slightly varied, the low-energy shapes of the time-averaged spectra were not so strongly affected (see Figure 3).

The highest and lowest 2–10 keV fluxes were $\sim 2.7 \times 10^{-11} \text{ erg s}^{-1} \text{ cm}^{-2}$ in epoch 4 and $\sim 0.3 \times 10^{-11} \text{ erg s}^{-1} \text{ cm}^{-2}$ in epoch 7, respectively. They are in a range of just 7%–70% of the 2–10 keV flux of $\sim 4.0 \times 10^{-11} \text{ erg s}^{-1} \text{ cm}^{-2}$ averaged over 1997–2002 (*RXTE* AGN Timing & Spectral Database; Maoz et al. 2002); thus NGC 3516 was in an X-ray faint phase during the present observations. Table 3 further gives the 2–10 keV fluxes of the hard PL continuum and the reflection components, calculated separately, after removing the absorption. The 2–10 keV light curves of the two spectral components, derived in this way, are presented in Figure 4(top). The time of each data point refers to the middle epoch (in MJD) of that observation as given in Table 1. Interest-

ingly, the flux of the reflection component significantly changed by a factor of 2 on a time scale of several months. However, the hard PL component varied almost by an order of magnitude or more in amplitude. Clearly, the large intensity change in Figure 2 was mostly carried by the hard PL variation. The largest flux change of the hard PL emission in 2–10 keV is $\sim 2.4 \times 10^{-11} \text{ erg s}^{-1} \text{ cm}^{-2}$ in difference, and a factor of ~ 18 between epoch 4 and 7.

For further information about the AGN activity in NGC 3516, we also performed the spectral analysis including the energy band below 2 keV. For this purpose we selected epoch 7, where the AGN was faintest. In fact, as shown in Figure 5, the spectrum on this occasion exhibits a prominent soft X-ray excess at $\lesssim 2 \text{ keV}$, which is much less prominent in the other epochs. In order to examine if the soft excess structure originates from the AGN activity, we fitted the 0.5–10 keV spectrum at epoch

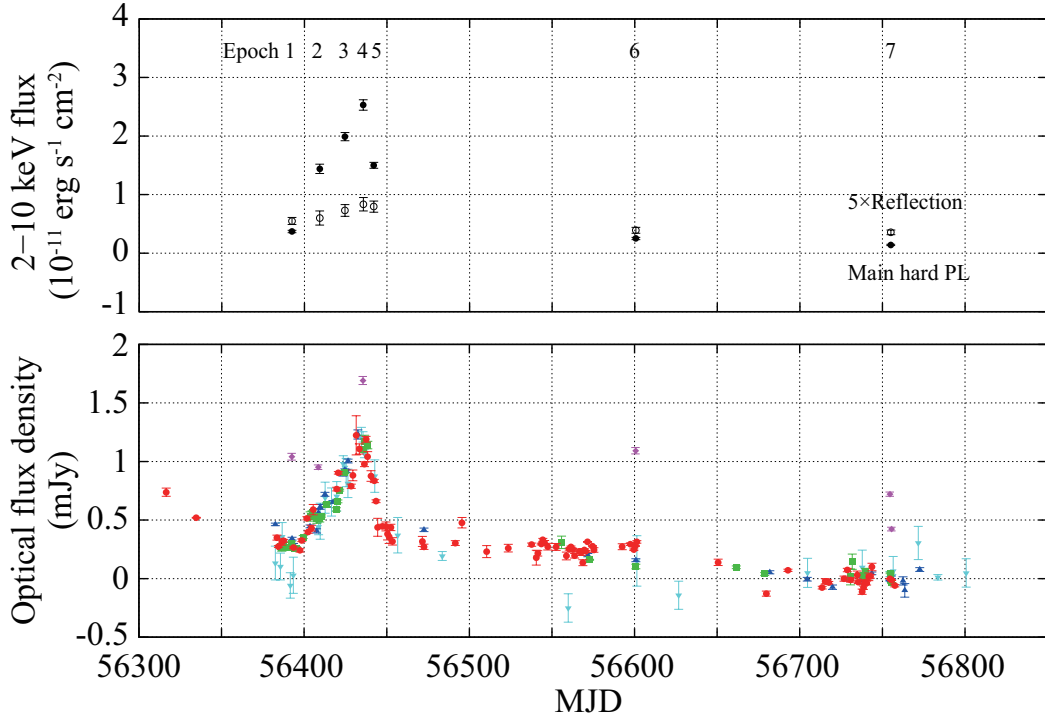


FIG. 4.— (Top) The 2–10 keV flux light curve of the main hard PL continuum (filled circles), and that of the reflection component including the Fe-K α line, after multiplying by 5 (open circles), both corrected for absorption. (Bottom) A light curve of the B -band flux density of the NGC 3516 nucleus, derived by applying the differential image photometry to the data of the Pirka (red), Kiso Schmidt (green), Nayuta (blue), and the Kanata telescope (cyan). The g' -band flux density obtained by the MITSuME telescope (magenta) is also plotted, with an offset of 0.5 mJy added after being scaled (see text).

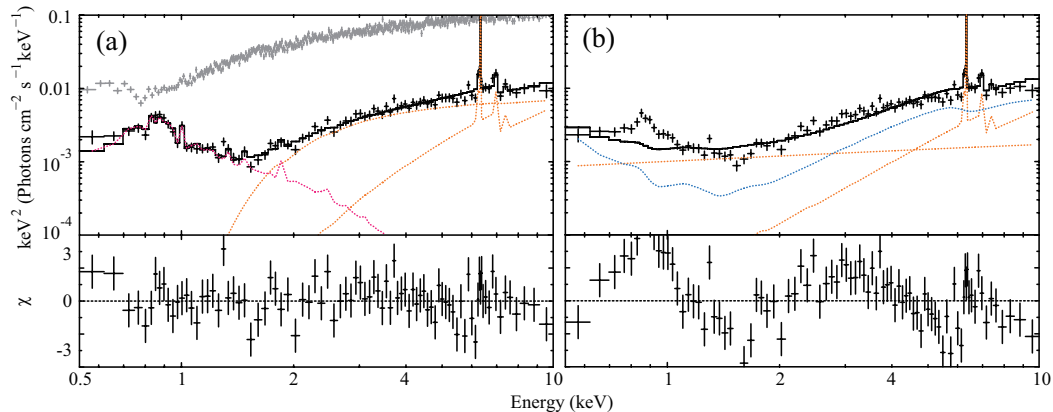


FIG. 5.— Examples for X-ray spectral analysis including the soft energy band below 2 keV. Black shows the 0.5–10 keV time-averaged spectrum at epoch 7 in a νF_ν form, fitted by `wabs * (cutoffpl + pexmon) + apec` (panel a) and `wabs * (cutoffpl + pexmon + kdblur * reflionx)` (panel b). Grey in panel (a) shows that at epoch 4 without fitting. In both panels, orange spectral components are same as those in Figure 3 except for absorption strength, while red in panel (a) and blue in panel (b) represent a galactic thin-thermal emission modeled by `apec` and a relativistically-blurred ionized reflection component modeled by `kdblur * reflionx`, respectively.

7 by two contrasting models; (a) `wabs * (cutoffpl + pexmon) + apec` and (b) `wabs * (cutoffpl + pexmon + kdblur * reflionx)`. In model (a), the soft excess is explained by `apec` (Smith et al. 2001) which represents thin-thermal plasma emission from the host galaxy, while in model (b) by a `kdblur * reflionx` model (Laor 1991; Ross & Fabian 2005) which describes relativistically-smearred reflection continuum. As a result, the fit with model (a) became successful with $\chi^2/\text{d.o.f.} = 100.3/84$ (Figure 5a), in which the soft excess, apparently involving emission lines, is reproduced by the plasma emission

model. On the other hand, the fits with model (b) was unsuccessful with $\chi^2/\text{d.o.f.} = 355.9/82$, mainly due to lack of the emission lines at ~ 0.85 keV and a convex data shape in the 2–5 keV band (Figure 5b). Therefore, the spectrum below 2 keV is dominated by the host galaxy emission, at least in epoch 7. This justifies us to limit the spectral studies to the energies above ~ 2 keV. Of course, the AGN emission, when bright, probably dominates down to ~ 0.5 keV, but is strongly affected by ionized-absorption features at ~ 0.8 keV, as shown in

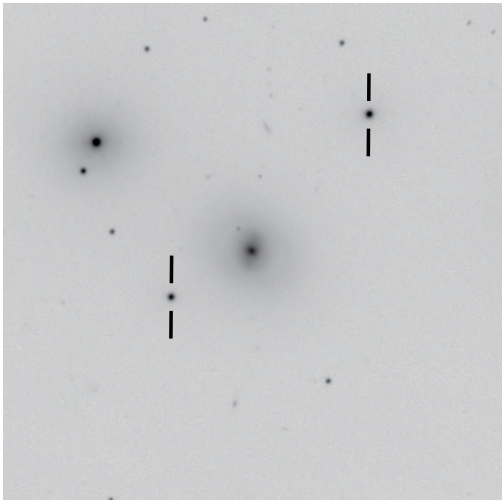


FIG. 6.— An example of B -band reference image of NGC 3516 for the DIP analysis of the MINT/Nayuta telescope data. It was obtained by stacking 65 images with an exposure of 60 seconds each taken on 2014 April 7, when the FWHM of the PSF was 1.8 arcsec. The two reference stars, marked by bars, were used for matching the photometric intensity and the PSF, and for the relative photometry of the AGN flux. North is up, east is left, the field of view of the image displayed is 6×6 arcmin², and the image intensity levels are displayed in a logarithmic scale. The NGC 3516 nucleus is near the image center.

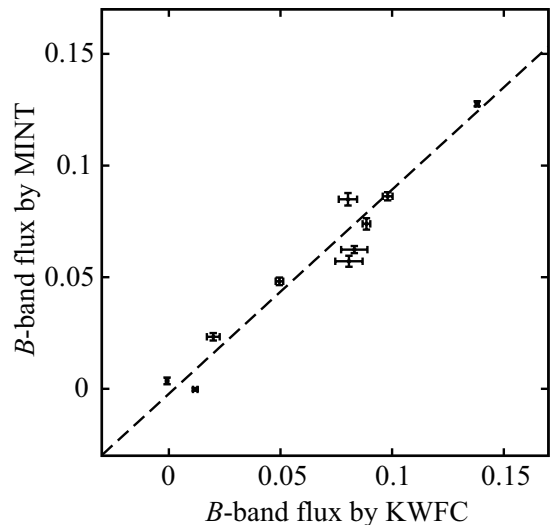


FIG. 7.— The B -band fluxes obtained by the KWFC/Kiso Schmidt telescope, compared with those from the MINT/Nayuta telescope on the same observing nights. The unit of flux is that of the average magnitude of the two nearby reference stars. The dashed line represents the best fit linear regression with an error added to the photometric errors by root-sum-square for the reduced χ^2 to achieve unity.

Figure 5(a).

3.2. Differential Imaging Photometry and Optical Light Curves

According to changes of the atmospheric seeing during an observation, the flux of an AGN within an aperture changes differently from that of the host galaxy, leading to a significant uncertainty in measuring the flux variation of a faint AGN hosted by a bright galaxy. To minimize such uncertainty in the photometry of the NGC

3516 nucleus, we therefore performed Difference Image Photometry (DIP; Crofts 1992; Tomaney & Crofts 1996). As presented in Figure 6 for example, a reference image was created by stacking many images obtained at the same night with good seeing condition. Then, we matched the position, the photometric intensity, and the point-spread function (PSF) of the reference image to those of each individual image and subtracted the former from the latter. Two nearby field stars, located at (Ra, Dec) = (11:06:28.51, +72:35:46.2) and (11:07:00.41, +72:33:33.3), were used as the reference to match the photometric intensity and the PSF. The IRAF *psfmatch* task was used for matching the PSFs. After that, for each individual image, the residual flux at the center of the galaxy was measured relative to the two nearby reference stars, with a circular aperture of $\phi = 4 \times$ full-width at half maximum (FWHM) of the PSF in diameter. Finally, the residual flux data at the same observing night were averaged to obtain the flux difference of the NGC 3516 nucleus at that epoch with respect to the reference image. The photometric error was estimated from the ensemble scatter of the DIP fluxes and the number of the images obtained at the same night. These procedures were applied to the data set of each telescope, individually.

Because the observing epochs of the reference images used in the DIP analysis depend on the telescopes, there can be systematic offsets between them. Systematic differences in the scaling factor among them are also possible because of the differences in the filter color term. To match the offset and the scaling factor among the four telescopes, we therefore performed a linear regression analysis to their B -band flux data sets of the same observing nights. An example, between two telescopes, is presented in Figure 7. The reduced χ^2 of the linear regression was much larger than unity when only the photometric errors were incorporated. Because this suggests the presence of some systematic errors, we added an error σ_{add} to the photometric errors in quadrature, and regarded it as the systematic error of the photometry. By requiring the reduced χ^2 to become unity, $\sigma_{\text{add}} \sim 0.06$ mJy was obtained.

The B - and V -band magnitudes of the two reference stars were calibrated relative to those of the more distant field stars whose magnitudes are presented in Sakata et al. (2010); these are based on the wide-field image data of the KWFC, in which both stars were observed simultaneously. The g' -band magnitudes of the reference stars were estimated from their B - and V -band magnitudes according to Jordi et al. (2006).

The light curves of the NGC 3516 nucleus, thus derived in the optical B and g' bands, are presented in the bottom panel of Figure 4, and the data are listed in Table 4, without correction for the Galactic extinction. They are both the differential fluxes with respect to the reference image obtained from the image data on 2014 April 08 (UTC), and the error bars of the data points do not include σ_{add} . The total numbers of the photometric data points are 180 and 6 for the B and the g' bands, respectively. As shown in Figure 4, the B -band flux varied rather similarly to that of the hard PL component in the 2–10 keV band. Although the number of the data points are small, the g' -band flux variation also followed them. The larger relative scatters of the g' -band

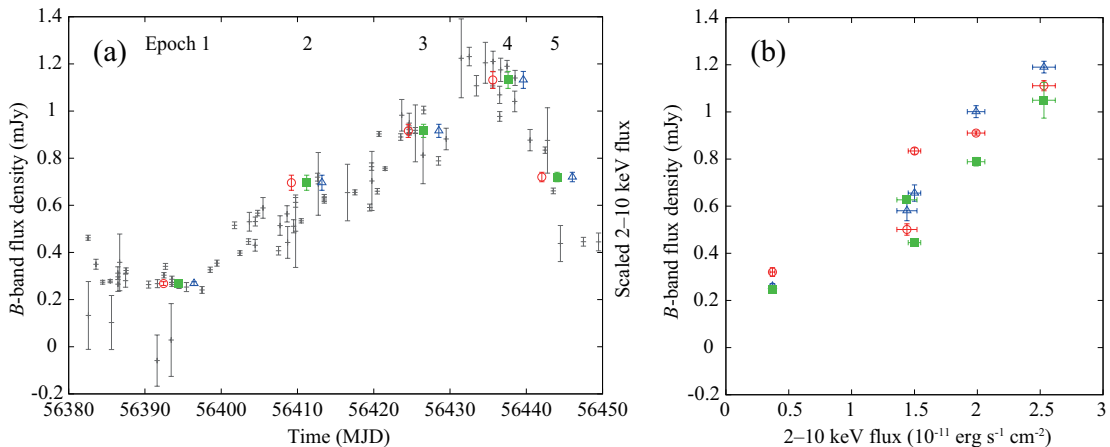


FIG. 8.— (a) Zoomed light curves of the B band (grey) and the 2–10 keV hard PL component (red circles) from epoch 1 to 5. Green squares and blue open triangles show the X-ray light curves which are purposely delayed by +2 and +4, respectively. The X-ray flux amplitude was scaled to match that in the B band. (b) A plot between the 2–10 keV hard PL flux and the B -band flux density, wherein an artificial time delay is applied to the X-ray data by 0 day (red circle), 2 days (green box), and 4 days (blue triangle).

TABLE 4
OPTICAL FLUXES

Observation Date (MJD)	Observatory ^a	Filter	Flux ^b (mJy)	Flux Error (mJy)
56316.544	P	B	0.738	0.035
56334.674	P	B	0.519	0.003
56382.554	N	B	0.462	0.011
56382.588	H	B	0.133	0.144
56383.576	P	B	0.350	0.021
56384.454	P	B	0.274	0.008
56385.448	K	B	0.278	0.007
56385.611	H	B	0.103	0.115
...
56392.487	K	B	0.303	0.011
56392.625	M	g'	0.541	0.029
56392.686	N	B	0.341	0.012
...

NOTE. — (This table is available in its entirety in a machine-readable form in the online journal. A portion is shown here for guidance regarding its form and content.)

^a Observatory code : P = the MSI at the Pirka telescope, M = the MITSuME, K = the KWFC at the Kiso Schmidt telescope, N = the MINT at the Nayuta telescope, and H = the HOWPol at the Kanata telescope.

^b The flux difference with respect to the reference image on 2014 April 08 (UTC).

data points are caused by the small telescope size and the large pixel scale of the camera (MITSuME) by which the data were obtained. These results indicate that the optical continuum and the 2–10 keV PL component varied in a good correlation with each other. Between the peak and bottom, the B -band flux density varied by ~ 1.2 mJy. After correcting for the Galactic extinction and the optical extinction of the NGC 3516 nucleus ($A_B \sim 1.3$ mag in total), it becomes ~ 4.0 mJy, corresponding to $\sim 2.7 \times 10^{-11}$ erg s $^{-1}$ cm $^{-2}$ in νF_ν units¹⁷.

¹⁷ There are different estimates for the optical extinction of the NGC 3516 nucleus: Cackett et al. (2007) estimated it at $E(B-V) = 0.15-0.16$ mag, which can be converted to $A_B = 0.62-0.66$ mag, and Denney et al. estimated it at $A_B = 1.68-1.72$ mag. We adopted their average here. Although the $N_H \sim 1-2 \times 10^{22}$ cm $^{-2}$ derived from the X-ray absorption suggests much larger optical extinction of $A_B \sim 10$ mag, AGNs often show smaller optical extinction than that converted from the X-ray N_H (e.g., Burtscher et al. 2015).

To complete this DIP analysis, the AGN flux at the faintest phase during our observation was estimated. We applied an aperture photometry to the stacked B -band image obtained on 2014 April 7 by the MINT attached on the Nayuta telescope (Figure 5), because it achieved, on this day, the best seeing among the four. Sakata et al. (2010) estimated the host galaxy flux in B band as 8.38 ± 0.18 mJy,¹⁸ within an aperture diameter of $\phi = 8.3$ arcsec with the sky reference of a $\phi = 11.1-13.9$ arcsec annulus. By applying the photometry with the same parameters, we obtained the B -band flux density of 8.44 mJy after the correction for the Galactic extinction, yielding the AGN flux of 0.1 ± 0.2 mJy. Considering the various systematic errors in the photometry, the B -band AGN flux at the faintest phase during the observations is estimated as about a few times 0.1 mJy, with a similar amount of flux error.

3.3. Time-Series Analysis on the Flux Variations of the Hard PL X-ray and the Optical Continuum

As shown in Figure 4, the optical flux changed almost simultaneously with the 2–10 keV hard PL flux. In order to examine possible time lags between them, we first focus on their expanded light curves from epoch 1 to 5, as presented in Figure 8(a). Clearly, the AGN became the brightest in both bands at epoch 4. Also plotted in the same figure is the X-ray light curve shifted by +2 days and +4 days. Apparently, the X-ray light curve with a few days shift shows the closest agreement with the B -band light curve, suggesting that the variation of the X-rays preceded that of the B band by a few days.

Figure 8(b) presents the correlation of the X-ray flux with 0, +2, and +4 days temporal shifts, against the B -band flux at the delayed epochs. The latter was estimated by averaging the B -band fluxes in close observations within ± 1 day. The correlation between those fluxes appears to be strongest when the X-ray light curve is shifted by +2 days. This reconfirms that the X-ray variations preceded that of the B band by a few days.

¹⁸ Since Sakata et al. (2010) assumed the Galactic extinction of $A_B = 0.183$ mag according to Schlegel, Finkbeiner & Davis (1998), we converted their host galaxy flux to that assuming $A_B = 0.151$ mag adopted in this paper.

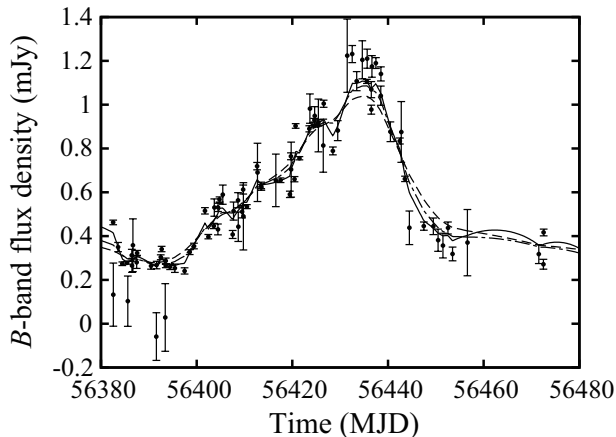


FIG. 9.— The observed B -band light curve (filled dots) and its interpolations used for the time-series analysis. The solid, dot-dashed, and dashed lines represent the best fit light curves based on the DRW models with $\sigma_{\text{add}} = 0.00$ mJy, 0.03 mJy and 0.06 mJy, respectively.

Below, let us quantify the suggested time lag with two methods.

3.3.1. Cross-correlation Analysis

One method is the interpolated cross-correlation function (ICCF) method, which has been widely used (White & Peterson 1994; Peterson et al. 1998). This is the same as the ordinary cross-correlation function (CCF), but either or both of the time-series data are interpolated, so that the CCF can be calculated even if the two data sets have different samplings, or when either or both are irregularly sampled.

Since the monitoring cadence of the B -band data was much higher than that of the X-ray data, only the B -band light curve was interpolated, to make it nearly continuous. The interpolated B -band light curve was calculated using a fitting code developed by Zu et al. (2011), which assumes a damped random walk (DRW) model for the flux variation. The DRW model has been demonstrated to be a good statistical model of flux variations of the UV-optical continuum emission of AGNs (e.g., Kelly et al. 2009; Kozłowski et al. 2010; MacLeod et al. 2010, 2012; Zu et al. 2013). In this interpolation, the systematic error σ_{add} of the photometry, either as determined in §3.2 or somewhat changed, was added in quadrature.

Figure 9 presents the observed B -band flux data and their interpolation. Thus, the interpolated light curve does not follow the observed data when $\sigma_{\text{add}} = 0.06$ mJy as determined in §3.2 is employed: the peak flux of the interpolated light curve was lower, and its flux decrease after the peak was slower. We generally found that a larger value of σ_{add} made the interpolated light curve smoother and less variable, probably because a larger σ_{add} would work as if applying a stronger low-pass filter. Therefore, we performed the CCF analysis using the B -band data with $\sigma_{\text{add}} = 0$ mJy in addition to 0.06 mJy to examine the possible uncertainty in lag caused by σ_{add} . As shown in Figure 9, the interpolated light curves then became to follow the observed data much better when σ_{add} is reduced.

The X-ray data of epoch 1–5 and the optical data of MJD = 56316–56511 were selected for the CCF analysis,

because the most remarkable flux variations were present in those epochs, and also because the B -band light curve data were sampled densely (Figure 4 and 8). The calculated CCFs, in which the B -band data were smoothed using $\sigma_{\text{add}} = 0$ mJy and 0.06 mJy, are presented in Figure 10, in which the time lag τ is defined to be positive if the optical precede X-rays. As shown in Figure 10, the CCF is peaked at about $\tau = -2$ days. This reconfirms the inference from Figure 8, and implies that the optical variation is delayed from that in X-rays by ~ 2 days. The CCF value at the peak is very high, > 0.98 , as indicated by Figure 8(b).

As quantitative measurement of τ , we use the centroid of the CCF peak, τ_{cent} , which is computed from all neighboring points around the CCF peak where CCF values are > 0.95 times that of the peak. The uncertainty of τ_{cent} is estimated using the model-independent Monte Carlo method of flux randomization and random subset sampling (FR/RSS) introduced by Peterson et al. (1998, 2004). The FR method modifies the observed fluxes in each realization randomly within the errors assigned to the individual data points, and the RSS method randomly extracts the same number of data points from the observed light curve allowing for multiple extraction. Then, the CCF and τ_{cent} are calculated for each realization in the same way, to produce the cross-correlation centroid distribution (CCCD). The CCCDs calculated by 5000 realizations with the FR/RSS method are presented in Figure 10, and the derived τ_{cent} and its uncertainties are listed in Table 5. Thus, the results with $\sigma_{\text{add}} = 0$ mJy and 0.06 mJy agree well with each other. On average, the lag has been estimated as $\tau_{\text{cent}} = -2.02^{+0.55}_{-0.50}$ days (1σ error), and the time lag is significantly non-zero, because the 99%-confidence limit is $\tau < -0.68$ days.

3.3.2. JAVELIN Analysis

The other method of the lag estimation is the JAVELIN software developed by Zu et al. (2011), which is widely employed not only in recent reverberation studies for the optical broad emission lines and the thermal dust emission of AGNs (e.g., Grier et al. 2012; Peterson et al. 2014; Koshida et al. 2014), but also in the lag analysis between flux variations of their X-ray emission and the UV-optical continuum emission (Shappee et al. 2014; McHardy et al. 2014; Lira et al. 2015). It explicitly builds a model of a response light curve that is expressed as a convolution of a source light curve by a top-hat transfer function with a certain lag, and fits the model to the data of flux variations in different bands, one as the source light curve and the others as the response light curves. The source light curve is modeled as a stochastic process using a DRW model, and the posterior distributions of the time lag as well as other model parameters are estimated using the Bayesian Markov Chain Monte Carlo (MCMC) method.

We use the B -band light curve as the source, whereas the X-ray data as the response, again with $\tau > 0$ meaning X-ray delays. The X-ray data of epoch 1–5 and the optical data of MJD = 56316–56511 were selected for the JAVELIN analysis, and $\sigma_{\text{add}} = 0$ mJy or 0.06 mJy was added to the B -band photometric errors in quadrature, just as in the CCF analysis. The posterior distribution of the time lag calculated by 250000 realizations of the

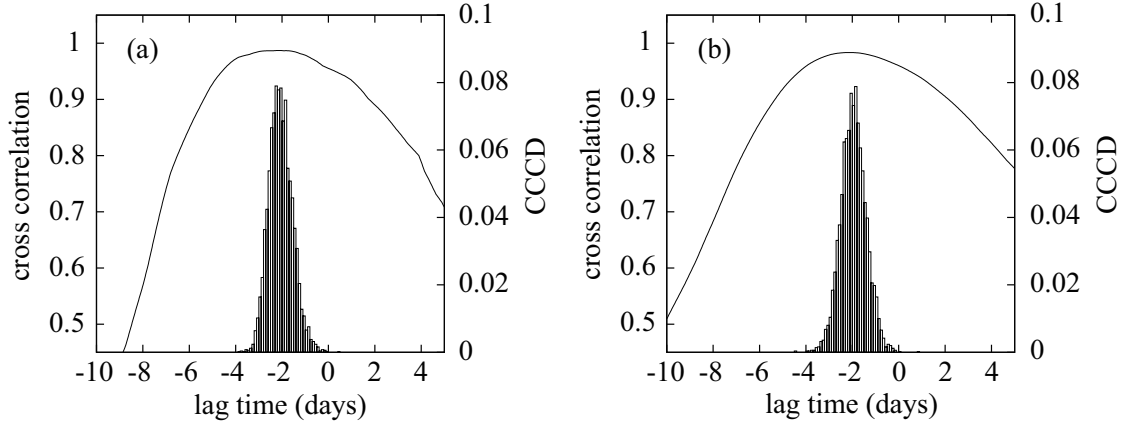


FIG. 10.— Results of the ICCF analysis between the flux variations of the 2–10 keV hard PL and the B -band flux density. The positive lag means that the optical leads X-rays. The solid line represents the cross correlation as a function of the time lag, and the histogram shows the distribution of the CCF centroid, τ_{cent} , obtained by 5000 realizations of the FR/RSS simulation. Panel (a) and (b) show the results with $\sigma_{\text{add}} = 0.00$ mJy and 0.06 mJy, respectively.

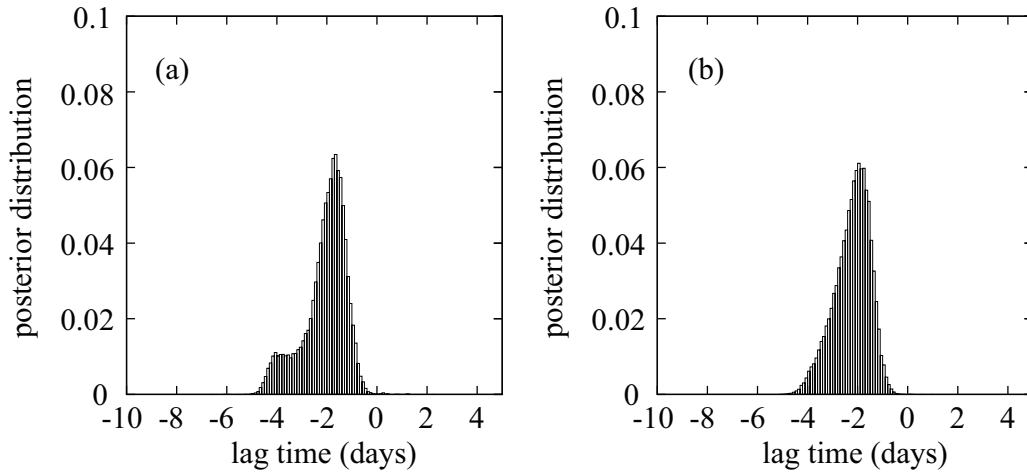


FIG. 11.— The same as Figure 10, but using the JAVELIN software.

TABLE 5
TIME LAG OF THE X-RAY FLUX VARIATION BEHIND THAT OF THE B BAND

analysis	$\sigma_{B,\text{sys}}^{\text{a}}$ (mJy)	lag time ^b (day)				
		1%	15.9%	50%	84.1%	99%
$\tau_{\text{cent}}^{\text{c}}$	0.00	-3.14	-2.56	-2.09	-1.54	-0.73
	0.06	-3.25	-2.49	-1.95	-1.41	-0.64
$\tau_{\text{JAV}}^{\text{d}}$	0.00	-4.42	-2.97	-1.90	-1.32	-0.66
	0.06	-4.07	-2.95	-2.12	-1.53	-0.90

^a The systematic error for the B -band photometries added to the flux errors in quadrature.

^b Percentiles.

^c The time lag based on the CCF analysis.

^d The time lag based on the JAVELIN software.

JAVELIN software are presented in Figure 11, and the resultant τ_{JAV} and its uncertainties are also listed in Table 5. The two values of σ_{add} again gave very similar results. The lag times were estimated as $\tau_{\text{JAV}} = -1.90^{+0.58}_{-1.07}$ days and $\tau_{\text{JAV}} = -2.12^{+0.59}_{-0.83}$ days (1σ error) with $\sigma_{\text{add}} = 0$

and 0.06, respectively. Again, we can exclude the case of $\tau = 0$, because the 99%-confidence limit is $\tau < -0.78$ days on average. In summary, the two methods have given consistent results.

3.4. The X-ray Reflection Component

As shown in Table 3 and Figure 4 (top), we found a significant flux variation in the X-ray reflection component as well, on a time scale of several months, although its variation amplitude is much smaller than that of the primary X-rays. This indicates that the source region of the reflection component has an extent on a scale of ~ 0.1 pc. Moreover, the flux variation of the reflection component slightly lags behind that of the hard PL component, on a scale of a week, or possibly larger because the X-ray sampling becomes very sparse after epoch 5.

According to the unified model of AGNs, the reflection component accompanied by the neutral Fe- $K\alpha$ line is supposed to arise from a dust torus, but different origins such as outer accretion disks, and the broad emission-line region are also suggested (e.g. Awaki et al. 1991; Yaqoob & Padmanabhan 2004; Nandra 2006; Jian et al. 2011;

Minezaki & Matsushita 2015; Gandhi et al. 2015). Interestingly, the reverberation studies of NGC 3516 yielded the dust lag of $\sim 50 - 70$ days (Koshida et al. 2014), and the lag of broad Balmer emission lines of $\sim 7 - 13$ days (Peterson et al. 2004; Denney et al. 2010). They are comparable to the time scale of the variation of the X-ray reflection, and its delay behind the hard PL component. In order to further examine the origin of the X-ray reflection component, a direct comparison of its variation with that of the dust emission and the broad Balmer emission lines would be necessary; this will be discussed in a forthcoming paper.

4. DISCUSSION AND CONCLUSION

4.1. Summary of the results

In the present study, we performed an X-ray–optical simultaneous monitoring of the type 1.5 Seyfert galaxy NGC 3516 with *Suzaku* and Japanese ground-based telescopes, the Pirka, Kiso schmidt, MITSuME, Nayuta, and Kanata telescopes. By applying the spectral fitting to the X-ray data and differential image photometry to the *B*-band images, and quantitatively comparing the X-ray and optical flux variations, we have obtained the following results.

- During our observations, NGC 3516 was in an X-ray-faint state. It was faintest in epoch 7, when the 2–10 keV flux became $\sim 0.21 \times 10^{-11}$ erg s $^{-1}$ cm $^{-2}$, which is just 5% of the average flux recorded in 1997–2002 with *RXTE*. Even when brightest (epoch 4), the 2–10 keV flux was $\sim 2.70 \times 10^{-11}$ erg s $^{-1}$ cm $^{-2}$, which is only 70% of the average in 1997–2002. The flux varied on time scales longer than \sim days, without any intraday changes.
- The 2–45 keV emission mainly consisted of two spectral components; a variable hard power-law continuum with a photon index of ~ 1.75 , and a reflection component with a prominent narrow Fe-K α emission line. Throughout the monitoring, the hard X-ray component kept almost the same spectral shape, and exhibited a peak-to-peak flux change by $\sim 2.5 \times 10^{-11}$ erg s $^{-1}$ cm $^{-2}$, or by about an order of magnitude.
- The *B*-band flux density varied by ~ 4.0 mJy in peak to peak, which translates to a flux change by $\sim 2.7 \times 10^{-11}$ erg s $^{-1}$ cm $^{-2}$ in νF_ν units, after correcting for the optical extinction. The *B*-band flux varied on time scales longer than \sim days, like those of the X-rays.
- X-ray and *B*-band flux correlation was significantly detected for the first time in NGC 3516. The flux changes of the hard X-ray component significantly preceded those in *B*-band by $2.0_{-0.6}^{+0.7}$ days (1σ error).

4.2. X-ray–optical correlation appearing only in faint state

By the previous monitoring of NGC 3516 conducted with *RXTE* and the Israeli *WISE* telescope in 1997–2002, no significant correlations were derived between X-ray and *B*-band flux variations, giving a cross correlation

coefficient of < 0.35 (Maoz et al. 2002). In contrast, we succeeded in detecting a significant correlation between them with a high cross correlation coefficient of > 0.95 . What is responsible for the clear difference? Maoz et al. (2002) argued that the lack of correlation might be due to absorption changes that are independent of the primary X-ray variations. However, the 2–10 keV flux varied during their monitoring by a factor of ~ 4 in peak to peak. Such a large change would be hardly explained by the so-far recored variations in the column density of optically-thick neutral absorbers (Turner et al. 2011). We hence suggest alternatively that the dominant X-ray variable component changed between the two monitoring campaigns.

Noda et al. (2013) discovered that the X-ray emission of NGC 3516 comprises at least two different primary continua with distinct spectral shape and flux variability; a flat ($\Gamma \sim 1.1$ – 1.7) and steep ($\Gamma \sim 2.3$) spectral continua, which we hereafter call the Hard and Gradually-varying Primary Component (HGPC), and the Soft and Rapidly-varying Primary Component (SRPC), respectively. Noda et al. (2013) showed that luminosities of the HGPC and SRPC were comparable in a bright state in 2005, when the absorption-corrected 2–10 keV total flux was $F_{\text{total}} \sim 3.5 \times 10^{-11}$ erg s $^{-1}$ cm $^{-2}$. In contrast, the 2009 *Suzaku* observation caught NGC 3516 in a faint state with $F_{\text{total}} \sim 1.1 \times 10^{-11}$ erg s $^{-1}$ cm $^{-2}$, wherein the variation was carried solely by a $\Gamma = 1.7$ PL which can be identified with the HGPC. Thus, there is a certain threshold in between these two flux values, say, at $F_{\text{th}} \sim 3 \times 10^{-11}$ erg s $^{-1}$ cm $^{-2}$; above F_{th} the HGPC and SRPC coexist, whereas only the HGPC remains below F_{th} . These two primary continua have also been identified in another Seyfert NGC 3227 (Noda et al. 2014):¹⁹ Their luminosity-dependent behavior was found to be very similar to that observed from NGC 3516. Namely, the HGPC was always present, whereas the SRPC appeared when the source was brighter than a certain threshold, to become co-existent with the other.

In the present *Suzaku* observations, the absorption-corrected 2–10 keV flux of NGC 3516 was in the range $(0.2 - 2.7) \times 10^{-11}$ erg s $^{-1}$ cm $^{-2}$, i.e., always below the suggested F_{th} . Furthermore, the 2–45 keV spectrum of the main variable PL was flat with $\Gamma \sim 1.75$, and the CCP distributions are smoothly connected to those in 2009 (Figure 2). Hence, we conclude that NGC 3516 was in the faint phase, with the HGPC dominating just as in the 2009 observation. On the other hand, during the 1997–2002 monitoring by Maoz et al. (2002), the averaged 2–10 keV flux was $F_{\text{total}} \sim 4.0 \times 10^{-11}$ erg s $^{-1}$ cm $^{-2}$ which is higher than F_{th} , indicating that NGC 3516 was mostly in the bright phase. If the SRPC has a significantly poorer correlation with the optical than the HGPC does, the correlation between the total X-ray flux and the optical should become worse when NGC 3516 is in the bright phase. Thus, the difference between Maoz et al. (2002) and ours may be explained by presuming that the HGPC is well correlated with the optical while the SRPC is not.

To generalize the above conclusion, we collected cross

¹⁹ The HGPC and the SRPC correspond to the Faint-branch Variable (FV) and the Bright-branch Variable (BV) components in Noda et al. (2014), respectively.

correlation coefficients (CCCs) from peak values of the CCF in previous simultaneous observations of various Seyferts. As a result, sources with high $L_{\text{bol}}/L_{\text{Edd}}$ ratios were found to have relatively low CCCs; MCG-6-30-15 with $L_{\text{bol}}/L_{\text{Edd}} \sim 0.2$ has $\text{CCC} \lesssim 0.1$ (Lira et al. 2015), NGC 4051 with $L_{\text{bol}}/L_{\text{Edd}} \sim 0.15$ has $\text{CCC} \sim 0.3$ (Breedt et al. 2009), and MR 2251-178 with $L_{\text{bol}}/L_{\text{Edd}} \sim 0.2$ has $\text{CCC} \sim 0.5$ (Arevalo et al. 2008). In contrast, sources with low $L_{\text{bol}}/L_{\text{Edd}}$ ratios possibly have high CCCs; NGC 6814 with $L_{\text{bol}}/L_{\text{Edd}} \sim 0.008$ has $\text{CCC} \sim 0.9$ (Troyer et al. 2015); and NGC 3516 in the present study has $\text{CCC} \gtrsim 0.95$ wherein $L_{\text{bol}}/L_{\text{Edd}} < 0.01$ is indicated by the value of 0.00612 (Vasudevan & Fabian 2009), obtained in 2001 when NGC 3516 showed F_{tot} close to the second highest among ours. Therefore, we speculate that X-ray–optical correlation in Seyfert galaxies becomes commonly worse when the Eddington ratio gets higher, because the SRPC start dominating.

According to Figure 12(b) and related descriptions in Noda et al. (2014), the SRPC may originate from patchy coronae heated by magnetic process on the surface of a disk (e.g., Reynolds & Nowak 2003). If covering fraction of the patchy coronae against the disk is small, the SRPC generated in the coronae can be related to just small areas of the disk, making X-ray and optical variations independent. Another possible origin of the SRPC is a faulty jet at the accretion axis of the SMBH (e.g., Ghisellini et al. 2004). If the jet emission region is located far away from the accretion disk as suggested by Noda et al. (2014), connection between the SRPC and the disk optical emission may become weaker, making their correlation poorer. In any case, the emergence and disappearance of these SRPC-generating regions are likely to be more localized effects than those responsible for the hard vs. soft state transitions seen in black-hole binaries, because the AGN state changes considered here take place on time scales of weeks to years, which are much shorter than would be expected (e.g., several ten thousand years) if the typical state-transition time scales, \sim days, are scaled to the mass ratios.

4.3. The origin of X-ray and optical correlation

4.3.1. Application of standard X-ray reprocess model

The measured optical lag of $2.0_{-0.6}^{+0.7}$ days strongly supports the X-ray reprocessing model (e.g., Krolik et al. 1991; Cackett et al. 2007); optical brightening occurred, at least in the present case, through irradiation by the increased hard X-ray intensity. This process is energetically feasible, because the 2–10 keV X-ray flux increase by $2.5 \times 10^{-11} \text{ erg s}^{-1} \text{ cm}^{-2}$ is comparable to the B -band flux increase by $\sim 2.7 \times 10^{-11} \text{ erg s}^{-1} \text{ cm}^{-2}$. The optical lag time in NGC 3516 obtained here is similar to those of a few days observed from other Seyfert galaxies, including NGC 5548 (e.g., Suganuma et al. 2006; Mchardy et al. 2014; Edelson et al. 2015), NGC 3783 (Arevalo et al. 2009), NGC 4051 (Breedt et al. 2010), and NGC 6418 (Troyer et al. 2015). Therefore, the suggested mechanism, i.e., the X-ray reprocessing, can be operating commonly among these Seyfert galaxies.

Let us, then, investigate whether or not the derived optical lag can be explained by the most commonly adopted X-ray reprocessing model (e.g., Cackett et al. 2007), which assumes that an optically-thick geometrically-thin

standard accretion disk continues down to the innermost last-stable circular orbit (ISCO), located at $3R_s$ where $R_s = 2GM_{\text{BH}}/c^2$ is the Schwarzschild radius and M_{BH} the black-hole mass, and is illuminated by a lamppost-type X-ray source proximate to the black hole. At radii $R \gg R_s$, the radial temperature profile of the disk is given as (Shakura & Sunyaev 1973)

$$T(R) = \left(\frac{3GM_{\text{BH}}\dot{M}}{8\pi\sigma} \right)^{\frac{1}{4}} R^{-\frac{3}{4}}, \quad (1)$$

where \dot{M} is the mass accretion rate, G is the gravitational constant, and σ is the Stefan-Boltzmann constant.

After the delay time τ , the X-ray flux variation that arose close to the black hole will propagate to a radius $R = c\tau$, and will increase the emissivity there. Let us define a wavelength $\lambda = hc/kT(c\tau)X$ in such a way that the continuum emission at this radius is peaked at λ , where X is a numerical factor of order unity. Although the Wien’s displacement law for a blackbody radiation in νB_ν gives $X = 3.92$, we here set $X \sim 3.2$, according to the detailed calculations of the disk response to continuum emission by Cackett et al. (2007) and Collier et al. (1999). Substituting $c\tau$ for R , and expressing $T(c\tau)$ with λ , eq. (1) can be rewritten as

$$T(R) = \frac{hc}{k\lambda X} \left(\frac{R}{c\tau} \right)^{-\frac{3}{4}}. \quad (2)$$

By eliminating $T(R) \cdot R^{3/4}$ from eq. (1) and eq. (2), we obtain $\dot{M} \propto M^{-1}\tau^3\lambda^{-4}$. Further expressing \dot{M} by the bolometric luminosity of the accretion disk, $L_{\text{bol}} \sim 0.1 \dot{M}c^2$ (assuming that the disk extends to the ISCO), and normalizing it to the Eddington luminosity ($\propto M_{\text{BH}}$), the Eddington ratio of the source η is estimated as

$$\eta \equiv L_{\text{bol}}/L_{\text{Edd}} \sim 3.8 \left(\frac{M_{\text{BH}}}{3.2 \times 10^7 M_\odot} \right)^{-2} \times \left(\frac{\tau}{2.0 \text{ day}} \right)^3 \left(\frac{\lambda}{0.44 \mu\text{m}} \right)^{-4}. \quad (3)$$

Equation (3), in fact, implies a serious problem. First of all, it indicates an unrealistic “super-Eddington” condition. Even putting aside this issue, it means a factor of ~ 500 discrepancy against the likely value of $\eta = 0.006 - 0.01$ (§ 4.2), which characterizes the NGC 3516 nucleus during the present observations. The difficulty can be more directly stated: by summing up the blackbody contributions from various disk annuli, the continuum spectrum from the accretion disk under consideration can be calculated as

$$f_\nu \sim 550 \text{ mJy} \left(\frac{\tau}{2.0 \text{ days}} \right)^2 \left(\frac{D}{41.3 \text{ Mpc}} \right)^{-2} \times \left(\frac{\lambda}{0.44 \mu\text{m}} \right)^{-3} \cos i, \quad (4)$$

where i is the disk inclination (Collier et al. 1999; Cackett et al. 2007). Thus, the measured delay predicts very bright optical emission, arising from the inner part of the accretion disk. In other words, the SMBH would have to

be accreting with a very high rate, in order for its accretion disk to emit the B -band light from such a large distance as ~ 2 light days. Equation (4) means a two-orders-of-magnitude contradiction to the present optical data, that the peak-to-peak flux variation in the B band was ~ 4.0 mJy, and the minimum B -band flux during the observation would be less than that. Inversely, if we started from the assumption of $\eta = 0.006 - 0.01$, the B -band lag predicted by eq.(3) would become ~ 8 times smaller than was measured. It is thus extremely difficult to reconcile the measured clear optical delay by ~ 2 days with the observed optical faintness, as long as we assume a standard disk extending down to the ISCO and an illuminating X-ray source close to the SMBH.

4.3.2. Consideration of the X-ray irradiation

In the X-ray reprocessing model, we should consider not only the viscous heating but also the heating by the X-ray irradiation. The former, which underlies eq.(1), is written as

$$D_{\text{vis}} = \frac{3GM_{\text{BH}}\dot{M}}{8\pi R^3} \quad , \quad (5)$$

whereas the latter is given as

$$D_{\text{irr}} = \frac{(1-A)L_{\text{X}}}{4\pi R_{\text{X}}^2} \cos\theta \quad , \quad (6)$$

where L_{X} is the X-ray luminosity, A is the disk albedo, R_{X} is the distance from the disk to the X-ray illuminator, and θ is the X-ray incidence angle onto the disk. Collier et al. (1999) and Cackett et al. (2007) assumed that the X-ray emitter is located on the rotating axis of the SMBH like a ‘‘lamppost’’ (Figure 12a), and its height H_{X} from the SMBH is much smaller than R ($H_{\text{X}} \ll R$). Under these assumptions, we obtain $R_{\text{X}} \sim R$ and $\cos\theta = H_{\text{X}}/\sqrt{R^2 + H_{\text{X}}^2} \sim H_{\text{X}}/R$. Then, D_{vis} and D_{irr} have just the same R -profile, and the total heating per unit disk face area, $D_{\text{tot}} = D_{\text{vis}} + D_{\text{irr}}$, is described as

$$D_{\text{tot}} = \frac{3GM_{\text{BH}}\dot{M}}{8\pi R^3} + \frac{(1-A)L_{\text{X}}H_{\text{X}}}{4\pi R^3} \quad . \quad (7)$$

As a result, the radial temperature profile of the disk is now given by

$$T(R) = \left[\frac{3GM_{\text{BH}}}{8\pi\sigma} \left\{ \dot{M} + \frac{2(1-A)L_{\text{X}}H_{\text{X}}}{3GM_{\text{BH}}} \right\} \right]^{\frac{1}{4}} R^{-\frac{3}{4}} \quad . \quad (8)$$

It exhibits the same R -dependence as the standard viscous disk, namely, $T \propto R^{-3/4}$. Furthermore, because of the $L_{\text{X}} \propto \dot{M}$ proportionality, we should use $\dot{M} + 2(1-A)L_{\text{X}}H_{\text{X}}/3GM_{\text{BH}}$ in place of \dot{M} when converting this expression into that of η as eq.(3). Consequently, the Eddington ratio η and the B -band flux density can be given by the same eq.(3) and eq.(4), respectively.²⁰ Thus, we encounter just the same problem as before, even when the X-ray irradiation is taken into account.

According to e.g., Cackett et al. (2007), McHardy et al. (2014), and Edelson et al. (2014), typical Seyfert galaxies including NGC 5548, NGC 4051, and Mrk 335 yielded

²⁰ The Eddington ratio would differ by a factor of order unity because the radial profile of the temperature of the irradiated disk would be somewhat different from that of the standard viscous disk at small radii.

τ that are a few times larger than those expected from their estimated η . According to Mogan et al. (2010), the accretion disk sizes of gravitationally lensed quasars are larger, by a factor of ~ 4 , than those expected from η , just like in the Seyfert galaxies. These subtle but systematic contradictions between the disk size and η have also been well known in the X-ray reprocessing scenario (e.g., Collier et al. 1999, Cackett et al. 2007). Recently, Troyer et al. (2015) reported that NGC 6814 exhibited τ which is ~ 40 times larger than that predicted from the estimated η . In the present case of NGC 3516, the measured vs. predicted difference in the optical delay amounts to a factor of ~ 10 , which is considerably larger than those of NGC 5548, NGC 4051, and Mrk 335. These systematic discrepancies imply that the lamppost-type X-ray irradiation geometry shown in Figure 12(a) has a common problem, which is considered to become more prominent towards lower luminosities, considering that NGC 3516 and NGC 6814 have both relatively low values of η . Thus, we need to revise the geometrical assumptions, in order to make τ and η consistent in low Eddington-ratio Seyfert galaxies.

4.3.3. Possible geometry of accretion flows in low Eddington-ratio Seyferts

What kind of geometry of the corona and the accretion disk can reconcile η and τ from the present study? The contradiction in the lamppost-type X-ray reprocessing model, revealed in §4.3.1, arises mainly because the observed luminosity is too low for the size of the accretion disk determined by the observed time lag. Conversely, the measured $\tau \sim 2$ days is too large to be explained by the standard scenario, given the very low luminosity. In this respect, it has been very essential that the present observations caught the object at a very faint state not only in X-rays but also in the optical band (see the final paragraph in §3.2). This indicates that the $\eta - \tau$ inconsistency cannot be solved even if considering an anisotropically-irradiating lamppost corona (Dabrowski et al. 1997) that would make the X-ray flux we observe much lower than that illuminating accretion disk. Hence, we need to consider other geometries of the corona and the accretion disk that can reconcile η and τ from the present study.

One possible variant of the lamppost-type scenario is to place the X-ray source at a large height from the SMBH, to achieve $H_{\text{X}} \sim 2$ light days. In this geometry, X-ray flux variations can still precede that in the optical. Furthermore, the inner part of the accretion disk can be made rather cool, because \dot{M} can be reduced and F_{irr} gets much smaller than that with the assumption of $H_{\text{X}} \ll R$. These would make the black body flux low enough to be consistent with the observed optical faintness. Such a lamppost-type corona with $H_{\text{X}} \lesssim R$ was suggested to form at the base of a jet moving away from a SMBH with relativistic speeds (e.g., Lohfink et al. 2013; Wilkins & Gallo 2015). However, the value of $H_{\text{X}} \sim 2$ light days, or $\sim 500 R_{\text{s}}$, which is required to explain the present results, is orders of magnitude larger than invoked in the previous studies. It would be highly unrealistic to assume that such an emission region forms at a height of $\sim 500 R_{\text{s}}$ in this radio-quiet object, and that the region radiates essentially the *entire primary X-ray emission* (§3.1). In addition, the X-ray emission mechanism from such a re-

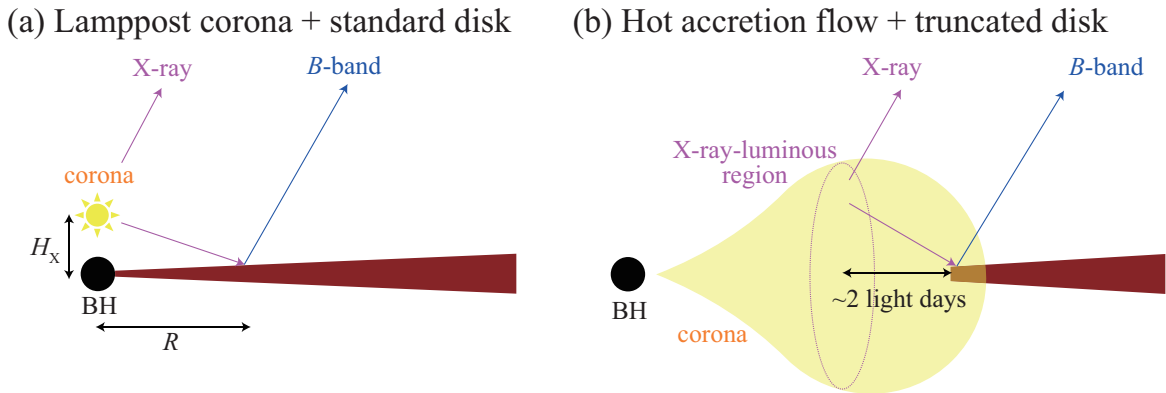


FIG. 12.— Schematic pictures of geometries of an accretion disk and a corona, in the lamppost configuration (panel a) and the model invoking a truncated disk and a hot accretion flow inside (panel b).

gion is problematic. As observed from BL-Lac objects, synchrotron radiation would give an X-ray spectral slope of $\Gamma \sim 2.5$ (e.g., Tanihata et al. 2004), which is much steeper than we observed ($\Gamma \sim 1.75$). Comptonization of soft photons from the accretion disk would produce *X-ray delays*, contrary to the observed optical delay. In short, this variant scenario fails to explain the present results.

As we noted repeatedly, the X-ray reprocessing model which has so far been considered (Figure 12a) assumes the optically-thick accretion disk to extend down to near the ISCO. However, it has long been known theoretically (e.g., Abramowicz et al. 1995) that a decreased luminosity, e.g., to $\eta \lesssim 0.01$, causes inner regions of such a disk to make a transition into an optically-thin and geometrically-thick hot flow. This will lead to a configuration shown in Figure 12(b); the disk is truncated at a radius much larger than the ISCO, and the accretion flow inside that radius may form a Radiatively Inefficient Accretion Flow, or RIAF (e.g., Yuan & Narayan 2014). Such bimodal behavior of accretion disks has been firmly verified through extensive observations of black-hole binaries (e.g., Done et al. 2007). The truncated disk picture has also been investigated by many authors, both observationally and theoretically, to explain low-luminosity AGNs (e.g. Ho 2008; Taam et al. 2012; Nemmen et al. 2014; and references therein). It is hence much more natural to try to explain the present results based on the geometry of Figure 12(b).

Referring to Figure 12(b), let us then consider an accretion disk that is truncated at a radius $R \gtrsim 2$ light days (or ~ 500 times their Schwarzschild radii) from the SMBH. Let us also assume that the accreting matter inside this radius forms a RIAF region, where the illuminating hard X-ray photons are produced via Comptonization (Noda et al. 2013a, 2014; Makishima et al. 2008; Yamada et al. 2013). In such a hot RIAF region, the electron density and temperature are theoretically predicted to increase inwards towards the SMBH (e.g., Esin et al. 1997), whereas the seed photon flux for inverse Comptonization obviously increases towards positions closer to the disk. Hence, the X-ray emissivity are considered to become maximum at a location in between the SMBH and the inner disk edge. Then, the optical delay of $\tau \sim 2$ days can be explained simply as the light travel time from the X-ray brightest regions to the inner

disk edge. Of course, this scenario requires a relatively low inclination, in order not to produce large differences in the light travel time to us, from the near side and far side of the disk; NGC 3516 may satisfy the condition, because of a relatively low inclination value of $i \sim 38^\circ$ (Wu & Han et al. 2001).

The truncated-disk picture can naturally explain, at the same time, the optical faintness, because the large amount of continuum radiation originating in the inner part of the accretion disk is no longer present. The *B*-band to X-ray flux ratio of NGC 3516 in these epochs is $\nu F_\nu(B)/F_X(2-10 \text{ keV}) \approx 1$. It is much lower than that of the composite spectrum for radio-quiet quasars (~ 6 ; Shang et al. 2011), but is consistent with those of the composite and model spectra for low-luminosity AGNs (Ho 2008; Nemmen et al. 2014). To be quantitative, let us assume, in eq. (6), $L_X = 5.2 \times 10^{42} \text{ erg s}^{-1}$, $A = 0$, $R_X = 2$ light days, and $\theta = \pi/4$. Then, the illuminating X-ray flux at a distance of 2.0 light days from the X-ray-bright region is calculated as $D_{\text{irr}} \sim 1.6 \times 10^{10} \text{ erg s}^{-1} \text{ cm}^{-2}$ during the peak of the flux variation. It predicts the disk temperature at the inner radius to be $\sim 4000\text{K}$ wherein *B*-band photons can be produced on the Wien side, even when the viscous heating is ignored in eq. (8). Incidentally, the disk temperature would increase by a factor of $(3/500)^{-3/4} \sim 45$ if the disk extended down to the ISCO.

As another merit of the truncated-disk scenario, the gradual X-ray variations without any intraday changes can be explained as well by the large volume of the RIAF region. In addition, the observed hard X-ray spectrum with $\Gamma \sim 1.7$ can be naturally explained as arising from the hot RIAF region via thermal Comptonization, as theoretically predicted (Esin et al. 1997), and observed from black-hole binaries (e.g., Makishima et al. 2008). Moreover, as shown in Figure 5, the soft X-ray band at epoch 7 was dominated by the galactic thin-thermal plasma emission, and no relativistically-smearing spectral components were required, also supporting that the standard accretion disk did not continue down to the ISCO. This scenario may be able to solve the τ vs. η conflict in the other low- η Seyferts as well, including NGC 6814 in particular (Troyer et al. 2015). We hence prefer the picture of the truncated disk and RIAF shown in Figure 12(b).

How does our model compare with other attempts on

the same subject? Recently, Gardner & Done (2016) proposed a model, that a geometrically-thick region, called the soft-excess region, is present at the inner edge of an accretion disk, and completely hides the hard X-ray corona. Far-ultraviolet photons, arising from the soft-excess region by the X-ray illumination, are reprocessed by optically-thick clouds distributing above the accretion disk, and produce optical variations. This model is different from ours in that X-rays from the corona cannot directly reach the accretion disk, and the optical variation is mainly due to the clouds rather than the disk. Presumably, our NGC 3516 results cannot be explained by the model of Gardner & Done (2016), because the 0.5–2 keV spectrum at epoch 7 is explained adequately by the galactic emission, without any strong soft excess resulting from the AGN activity. Therefore, we prefer our model (Figure 12b) to theirs.

For some quasars, it is claimed that the accretion disks, as measured by the UV-optical microlensing observations, are generally several times larger than those predicted by the standard accretion disk model (e.g., Morgan et al. 2010). These measurements are thought to be observing the unexpectedly large disk size like those revealed by the X-ray-to-optical continuum reverberation mapping for nearby Seyfert galaxies (e.g., Edelson et al. 2015, McHardy et al. 2016). Dexter & Agol (2011) suggested that the large disk size of quasars from microlensing is due to stochastic and strong local temperature fluctuations on the effective temperature profile of the standard accretion disk. Their inhomogeneous disk model is designed to enhance the flux contribution from outer disk radii, and thus make the disk half-light radius larger than the predictions of the standard accretion disk. However, their model, which does not consider the X-ray emission and attributes all UV-optical variability to the assumed temperature fluctuations, cannot explain the strong X-ray vs. optical correlations observed in NGC 3516 and other Seyfert galaxies. Furthermore, Kokubo (2015) showed that the disk model in Dexter &

Agol (2011) cannot explain, either, the tight inter-band correlations often observed in the optical light curves of quasars. Therefore, we do not discuss about the model any further.

For further refinement of the truncated-disk model, and its demarcation from the large- H_X model, correlations and time lags among different optical bands, including U , V , and R bands become important (e.g., Kokubo et al. 2014; Edelson et al. 2015; Fausnaugh et al. 2015; Kokubo 2015). These will be discussed in elsewhere.

4.4. Conclusion

The present coordinated X-ray and optical observations of NGC 3516 found the object in a very faint state in both wavelengths. A tightly correlated intensity change lasting for ~ 60 days was detected, wherein the optical B -band variation showed a clear delay by ~ 2 days behind that of the X-ray continuum which is described by a power-law model with $\Gamma \sim 1.7$. This optical lag indicates the effect of X-ray reprocessing, but the delay cannot be reconciled with the B -band faintness, as long as we consider the standard reprocessing scenario which invokes a standard accretion disk irradiated by a lamppost-type X-ray source. Instead, the observed results can be consistently explained assuming that the disk is truncated at $\sim 500 R_s$, and turns into a RIAF where the illuminating hard X-rays are produced via thermal Comptonization.

ACKNOWLEDGEMENT

We thank the referee for his/her valuable comments and suggestions. This work was partly supported by the Grants-in-Aid with grant numbers 26800095 (HN), 25287062 (TM), and 15J10324 (MK), from the Japan Society for the Promotion of Science (JSPS). HN was supported by the Special Postdoctoral Researchers Program in RIKEN.

REFERENCES

- Abramowicz, M. A., Chen, X., Kato, S., Lasota, J.-P., & Regev, O. 1995, *ApJ*, 438, L37
- Arévalo, P., Uttley, P., Lira, P., et al. 2009, *MNRAS*, 397, 2004
- Arévalo, P., Uttley, P., Kaspi, S., et al. 2008, *MNRAS*, 389, 1479
- Awaki, H., Koyama, K., Inoue, H., & Halpern, J. P. 1991, *PASJ*, 43, 195
- Balbus, S. A., & Hawley, J. F. 1991, *ApJ*, 376, 214
- Boldt, E., 1987, *Phys. Rep.*, 146, 215
- Breedt, E., McHardy, I. M., Arévalo, P., et al. 2010, *MNRAS*, 403, 605
- Burtscher, L., Davies, R. I., Gracia-Carpio, J., et al. 2015, accepted for publication by *A&A* (arXiv:1511.05566)
- Cackett, E. M., Horne, K., & Winkler, H. 2007, *MNRAS*, 380, 669
- Costantini, E., Nicastro, F., Fruscione, A., et al. 2000, *ApJ*, 544, 283
- Crotts, A. P. S. 1992, *ApJ*, 399, L43
- Dabrowski, Y., Fabian, A. C., Iwasawa, K., Lasenby, A. N., & Reynolds, C. S. 1997, *MNRAS*, 288, L11
- Dauser, T., Garcia, J., Wilms, J., et al. 2013, *MNRAS*, 430, 1694
- Denney, K. D., Peterson, B. M., Pogge, R. W., et al. 2010, *ApJ*, 721, 715
- Dexter, J., & Agol, E. 2011, *ApJ*, 727, L24
- Dickey, J. M., & Lockman, F. J. 1990, *ARA&A*, 28, 215
- Edelson, R., Gelbord, J. M., Horne, K., et al. 2015, *ApJ*, 806, 129
- Elvis, M., Wilkes, B. J., McDowell, J. C., et al. 1994, *ApJS*, 95, 1
- Esin, A. A., McClintock, J. E., & Narayan, R. 1997, *ApJ*, 489, 865
- Fabian, A. C., Miniutti, G., Gallo, L., et al. 2004, *MNRAS*, 353, 1071
- Fausnaugh, M. M., Denney, K. D., Barth, A. J. et al. 2015, arXiv:1510.05648
- Fukazawa, Y., Mizuno, T., Watanabe, S., et al. 2009, *PASJ*, 61, 17
- Gandhi, P., Hönic, S. F., & Kishimoto, M. 2015, *ApJ*, 812, 113
- Gardner, E., & Done, C. 2016, arXiv:1603.09564
- Gaskell, C. M., & Peterson, B. M., 1987, *ApJS*, 65, 1
- Gaskell, C. M. 2006, *Astronomical Society of the Pacific Conference Series*, 360, 111
- George, I. M., Turner, T. J., Netzer, H., et al. 2002, *ApJ*, 571, 265
- Ghisellini, G., Haardt, F., & Matt, G. 2004, *A&A*, 413, 535
- Gierliński, M., & Done, C. 2004, *MNRAS*, 349, L7
- Grier, C. J., Peterson, B. M., Pogge, R. W., et al. 2012, *ApJ*, 755, 60
- Gruber, D. E., Matteson, J. L., Peterson, L. E., & Jung, G. V. 1999, *ApJ*, 520, 124
- Ho, L. C. 2008, *ARA&A*, 46, 475
- Ishisaki, Y., Maeda, Y., Fujimoto, R., et al. 2007, *PASJ*, 59, S113
- Jiang, P., Wang, J., & Shu, X. 2011, *SCPMA*, 54, 1354
- Jordi, K., Grebel, E. K., & Ammon, K. 2006, *A&A*, 460, 339
- Kawabata, K. S., Nagae, O., Chiyonobu, S., et al. 2008, in *Society of Photo-Optical Instrumentation Engineers (SPIE) Conference Series*, Vol. 7014, *Society of Photo-Optical Instrumentation Engineers (SPIE) Conference Series*
- Kokubo, M., Morokuma, T., Minezaki, T., et al. 2014, *ApJ*, 783, 46

- Kokubo, M. 2015, *MNRAS*, 449, 94
- Koshida, S., Minezaki, T., Yoshii, Y., et al. 2014, *ApJ*, 788, 159
- Kotani, T., Kawai, N., Yanagisawa, K., et al. 2005, *Nuovo Cimento C Geophysics Space Physics C*, 28, 755
- Koyama, K., Tsunemi, H., Dotani, T., et al. 2007, *PASJ*, 59, 23
- Krolik, J. H., Horne, K., Kallman, T. R., et al. 1991, *ApJ*, 371, 541
- Laor, A. 1991, *ApJ*, 376, 90
- Lira, P., Arévalo, P., Uttley, P., McHardy, I. M. M., & Videla, L. 2015, *MNRAS*, 454, 368
- Lobban, A. P., Reeves, J. N., Porquet, D., et al. 2010, *MNRAS*, 408, 551
- Machida, M., Hayashi, M. R., & Matsumoto, R. 2000, *ApJ*, 532, L67
- Makishima, K., Takahashi, H., Yamada, S., et al. 2008, *PASJ*, 60, 585
- Maoz, D., Markowitz, A., Edelson, R., & Nandra, K. 2002, *AJ*, 124, 1988
- McHardy, I. M., Cameron, D. T., Dwelly, T., et al. 2014, *MNRAS*, 444, 1469
- McHardy, I., Connolly, S., Peterson, B., et al. 2016, [arXiv:1601.00215](https://arxiv.org/abs/1601.00215)
- Malizia, A., Molina, M., Bassani, L., et al. 2014, *ApJ*, 782, L25
- Morgan, C. W., Kochanek, C. S., Morgan, N. D., & Falco, E. E. 2010, *ApJ*, 712, 1129
- Morrison, R., & McCammon, D. 1983, *ApJ*, 270, 119
- Minezaki, T., & Matsushita, K. 2015, *ApJ*, 802, 98
- Miniutti, G., & Fabian, A. C. 2004, *MNRAS*, 349, 1435
- Mitsuda, K., Bautz, M., Inoue, H., et al. 2007, *PASJ*, 59, 1
- Miyakawa, T., Ebisawa, K., & Inoue, H. 2012, *PASJ*, 64, 140
- Nandra, K., Le, T., George, I. M., et al. 2000, *ApJ*, 544, 734
- Nandra, K. 2006, *MNRAS*, 368, 62
- Nandra, K., O'Neill, P. M., George, I. M., & Reeves, J. N. 2007, *MNRAS*, 382, 194
- Narayan, R., & Yi, I. 1994, *ApJ*, 428, L13
- Nemmen, R. S., Storchi-Bergmann, T., & Eracleous, M. 2014, *MNRAS*, 438, 2804
- Noda, H., Makishima, K., Uehara, Y., et al. 2011a, *PASJ*, 63, 449
- Noda, H., Makishima, K., Yamada, S., et al. 2011b, *PASJ*, 63, S925
- Noda, H., Makishima, K., Nakazawa, K., & Yamada, S. 2013a, *ApJ*, 771, 100
- Noda, H., Makishima, K., Nakazawa, K., et al. 2013b, *PASJ*, 65, 4
- Noda, H., Makishima, K., Nakazawa, K., & Yamada, S. 2013c, *Mem. Soc. Astron. Italiana*, 84, 707
- Noda, H., Makishima, K., Yamada, S., et al. 2014, *ApJ*, 794, 2
- Ozaki, S. 2005, *Annual Report of the Nishi-Harima Astronomical Observatory (ISSN 0917-6926)*, No. 15, p. 6–14 (2005), 15, 6
- Pei, L., Barth, A. J., Aldering, G. S., et al. 2014, *ApJ*, 795, 38
- Peterson, B. M., Wanders, I., Horne, K., Collier, S., Alexander, T., Kaspi, S., & Maoz, D., 1998, *PASP*, 110, 660
- Peterson, B. M. et al., 2004, *ApJ*, 613, 682
- Peterson, B. M., Ferrarese, L., Gilbert, K. M., et al. 2004, *ApJ*, 613, 682
- Peterson, B. M., Grier, C. J., Horne, K., et al. 2014, *ApJ*, 795, 149
- Reis, R. C., & Miller, J. M. 2013, *ApJ*, 769, LL7
- Reynolds, C. S., & Nowak, M. A. 2003, *Phys. Rep.*, 377, 389
- Rivers, E., Markowitz, A., & Rothschild, R. 2013, *ApJ*, 772, 114
- Ross, R. R., & Fabian, A. C. 2005, *MNRAS*, 358, 211
- Sakata, Y., Minezaki, T., Yoshii, Y., Kobayashi, Y., Koshida, S., Aoki, T., Enya, K., Tomita, H., Suganuma, M., Katsuno Uchimoto, Y., & Sugawara, S. 2010, *ApJ*, 711, 461
- Sako, S., Aoki, T., Doi, M., et al. 2012, *Proc. SPIE*, 8446, 84466L
- Schlafly, E. F., & Finkbeiner, D. P. 2011, *ApJ*, 737, 103
- Schlegel, D. J., Finkbeiner, D. P., & Davis, M. 1998, *ApJ*, 500, 525
- Shakura, N. I., & Sunyaev, R. A. 1973, *A&A*, 24, 337
- Shang, Z., Brotherton, M. S., Wills, B. J., et al. 2011, *ApJS*, 196, 2
- Shappee, B. J., Prieto, J. L., Grupe, D., et al. 2014, *ApJ*, 788, 48
- Smith, R. K., Brickhouse, N. S., Liedahl, D. A., & Raymond, J. C. 2001, *ApJ*, 556, L91
- Suganuma, M., Yoshii, Y., Kobayashi, Y., et al. 2004, *ApJ*, 612, 113
- Suganuma, M., Yoshii, Y., Kobayashi, Y., et al. 2006, *ApJ*, 639, 46
- Taam, R. E., Liu, B. F., Yuan, W., & Qiao, E., 2012, *ApJ*, 759, 65
- Takahashi, T., Abe, K., Endo, M., et al. 2007, *PASJ*, 59, 35
- Terashima, Y., Iyomoto, N., Ho, L. C., & Ptak, A. F. 2002, *ApJS*, 139, 1
- Tomaney, A. B., & Crotts, A. P. S. 1996, *AJ*, 112, 2872
- Tanihata, C., Kataoka, J., Takahashi, T., & Madejski, G. M. 2004, *ApJ*, 601, 759
- Troyer, J., Starkey, D., Cackett, E., et al. 2015, [arXiv:1509.01124](https://arxiv.org/abs/1509.01124)
- Turner, T. J., George, I. M., Nandra, K., & Mushotzky, R. F. 1997, *ApJ*, 488, 164
- Turner, T. J., Miller, L., Kraemer, S. B., & Reeves, J. N. 2011, *ApJ*, 733, 48
- Uttley, P., Edelson, R., McHardy, I. M., Peterson, B. M., & Markowitz, A. 2003, *ApJ*, 584, L53
- Uttley, P., Cackett, E. M., Fabian, A. C., Kara, E., & Wilkins, D. R. 2014, *A&A Rev.*, 22, 72
- Uttley, P., & Casella, P. 2014, *Space Sci. Rev.*, 183, 453
- Vasudevan, R. V., & Fabian, A. C. 2009, *MNRAS*, 392, 1124
- Watanabe, M., Takahashi, Y., Sato, M., et al. 2012, in *Society of Photo-Optical Instrumentation Engineers (SPIE) Conference Series*, Vol. 8446, *Society of Photo-Optical Instrumentation Engineers (SPIE) Conference Series*
- White, R. J., & Peterson, B. M., 1994, *PASP*, 106, 879
- Wu, X.-B., & Han, J. L. 2001, *ApJ*, 561, L59
- Yamada, S., Makishima, K., Done, C., et al. 2013, *PASJ*, 65, 1
- Yaqoob, T., & Padmanabhan, U. 2004, *ApJ*, 604, 63
- Yuan, F., & Narayan, R. 2014, *ARA&A*, 52, 529
- Zu, Y., Kochanek, C. S., & Peterson, B. M. 2011, *ApJ*, 735, 80
- Zu, Y., Kochanek, C. S., Kozłowski, S., & Udalski, A. 2013, *ApJ*, 765, 106